



### **Evaluating Welding Wire Fillers Derived from Scrap Aluminum**

The microstructure and age-hardening response of a scrap-derived aluminum filler processed with gas tungsten arc directed energy deposition was evaluated

BY J. HAMILTON, J. E. CARSLEY, AND J. KLEMM-TOOLE

### **Abstract**

There is a clear need for sustainable material production to reduce waste and improve efficiency. Incorporating recycled scrap into aluminum production can improve sustainability. However, with each successive recycling iteration, the aluminum scrap accumulates elements such as Si, Fe, and Cu that degrade recyclability. This paper explores using an end-of-life aluminum scrap stream, called twitch, to make a wire feedstock for welding and additive manufacturing. A composition was selected from the twitch composition space based on predictions of solidification cracking susceptibility and potential age-hardening response. Cu and Si contents were predicted to have the largest influence on cracking, and susceptibility was predicted to be reduced at contents greater than 2.5 wt-% Cu and 0 wt-% Si. Powder core tubular wire was produced based on the target composition and used to make gas tungsten arc directed energy deposition builds. Secondary phases predicted by the thermodynamic simulations were generally observed experimentally, namely  $\alpha$ -Al<sub>45</sub>(Fe, Mn)<sub>2</sub>Si<sub>2</sub>,  $Q-Al_5Cu_2Mg_8Si_6$ ,  $\theta-Al_2Cu$ , and Si. The alloy exhibited an age-hardening response when heat-treated at 190°C, resulting in a peak hardness between 110 and 120 HV, comparable to 6061. This work shows great potential for designing new welding and additive manufacturing fillers from the aluminum scrap stream.

### **Keywords**

- Arc Wire Directed Energy Deposition
- Additive Manufacturing
- Sustainability
- Aluminum Scrap

### Introduction

Aluminum is a highly recyclable and versatile material (Refs. 1, 2). It can be challenging to separate various aluminum alloys and non-ferrous alloy systems that get caught in the same recycling stream (Ref. 1). Therefore, with each successive recycling step, elemental constituents accumulate and degrade the usefulness of the scrap stream (Ref. 3). Twitch is a scrap stream that consists primarily of shredded wrought and cast aluminum with ferrous inclusions and is considered to be in its end-of-life state (Refs. 1, 2). Finding valuable use for end-of-life scrap streams, like twitch, poses an opportunity for the metallurgy community to improve the sustainability of structural alloys (Ref. 2).

Twitch is a recycling stream that has accumulated a series of elements, like Si and Fe, which are highly insoluble in the aluminum matrix (Refs. 1, 4, 5), as well as elevated amounts of Cu, Mn, and Mg (Ref. 6), which are commonly present in aluminum alloys. The elevated amounts of Si, Fe, Cu, Mn, and Mg significantly affect the phases present in a composition within the twitch scrap stream (Ref. 5). When the total Fe plus Mn content exceeds 0.8 wt-\%, primary  $\alpha$ -Al<sub>15</sub>(Fe, Mn)<sub>2</sub>Si<sub>2</sub> forms during solidification in a script-like morphology alongside hexagonal-shaped globules (Refs. 5, 7–9). The  $\alpha$ -phase may have some strengthening effect at the expense of ductility through grain size control, as  $\alpha$  particles may act as sites for Al nucleation, although the machinability is reportedly degraded (Refs. 7, 10). The α-phase has a complex body-centered cubic crystal structure formed by peritectic reactions during solidification (Refs. 11–13).

Other possible intermetallic compounds present in an alloy derived from the twitch scrap stream include Q-A<sub>5</sub>Cu<sub>2</sub>Mg<sub>8</sub>Si<sub>6</sub> and θ-Al<sub>2</sub>Cu (Ref. 5). Q has a hexagonal crystal structure and grows alongside  $\theta$  near the end of solidification (Refs. 5, 7, 14). The Q-phase is typically reported to have a globular morphology after solidification, which often becomes needle-like with aging heat treatments (Refs. 5, 15). The Q-phase can precipitate in a sequence including Q' and Q" in the solid state, though it is complex and poorly understood (Ref. 16). θ often forms as small, round particles in the aluminum matrix (Refs. 5, 17) and often nucleates at grain boundaries during terminal solidification (Ref. 18). Like the Q-phase,  $\theta$  can also form in a sequence in the solid state: supersaturated solid solution  $\rightarrow$ GP (Guinier-Preston) I zone  $\rightarrow \theta$ " (GP II zone)  $\rightarrow \theta$ '  $\rightarrow \theta$  (Ref. 19).  $\theta$  and  $\theta$ ' are the most stable, and  $\theta$ ' is the primary strengthening phase in Cu-bearing aluminum alloys (Ref. 20). Q" rods have been reported to promote nucleation of  $\theta$ ', subsequently refining the  $\theta$ ' plates compared to Si-free alloys (Refs. 16, 21).

One route to utilize the twitch scrap stream is to produce a feedstock for welding and/or additive manufacturing (AM) (AW-DED), which employs commonly available arc welding equipment, has become more popular as AM has the potential to reduce waste by minimizing the need for machining (Ref. 22) of near-net shape final products. When designing a wire

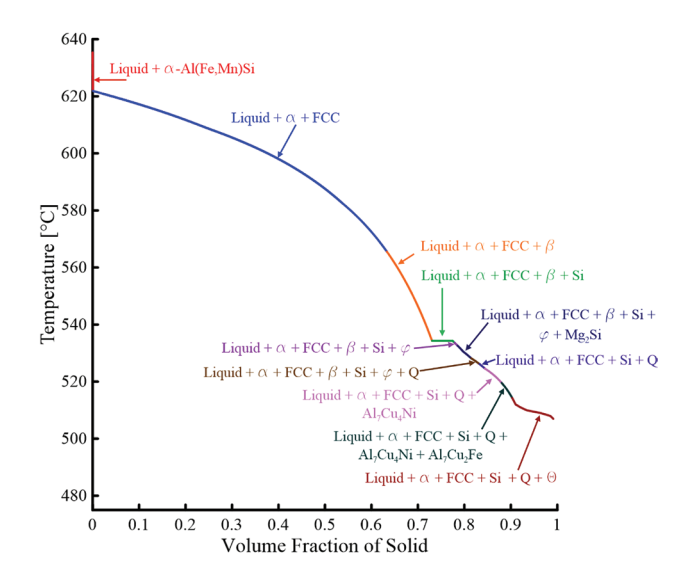


Fig. 1 — A Gulliver-Scheil simulation showing the solidification path for the average twitch composition listed in Table 1.

Table 1 — Average and Composition Range of Twitch Determined by X-Ray Fluorescence (XRF)											
Element	Si	Fe	Cu	Mn	Mg	Cr	Ni	Zn	Ti	Al	
Range (wt-%)	1–9	0.3-0.7	0.3-4	0.09-0.4	0.3-12	0-0.1	0-0.3	0.1–3	0-0.1	Bal.	
Average (wt-%)	5.28	0.53	1.63	0.24	1.79	0.04	0.07	1.06	0.04	Bal.	

Table 2 — Compositions for the Powders and Sheaths Used to Produce Powder-Core Tubular Wire of the Twitch Alloy

	Compositions (wt-%)										
	Al	Si	Fe	Cu	Mn	Mg	Cr	Ni	Zn	Ti	
Al-Si Powder	88	12	-	-	-	-	-	-	-	-	
Fe-Al Powder	8.67	0.04	90.78	0.18	0.06	0	0.06	0.01	0	0.01	
NiAl3 Powder	57.97	-	-	-	-	-	-	42.03	-	-	
2024 Sheath	92.05	0.5	0.5	4.35	0.6	1.5	0.1	0	0.25	0.15	

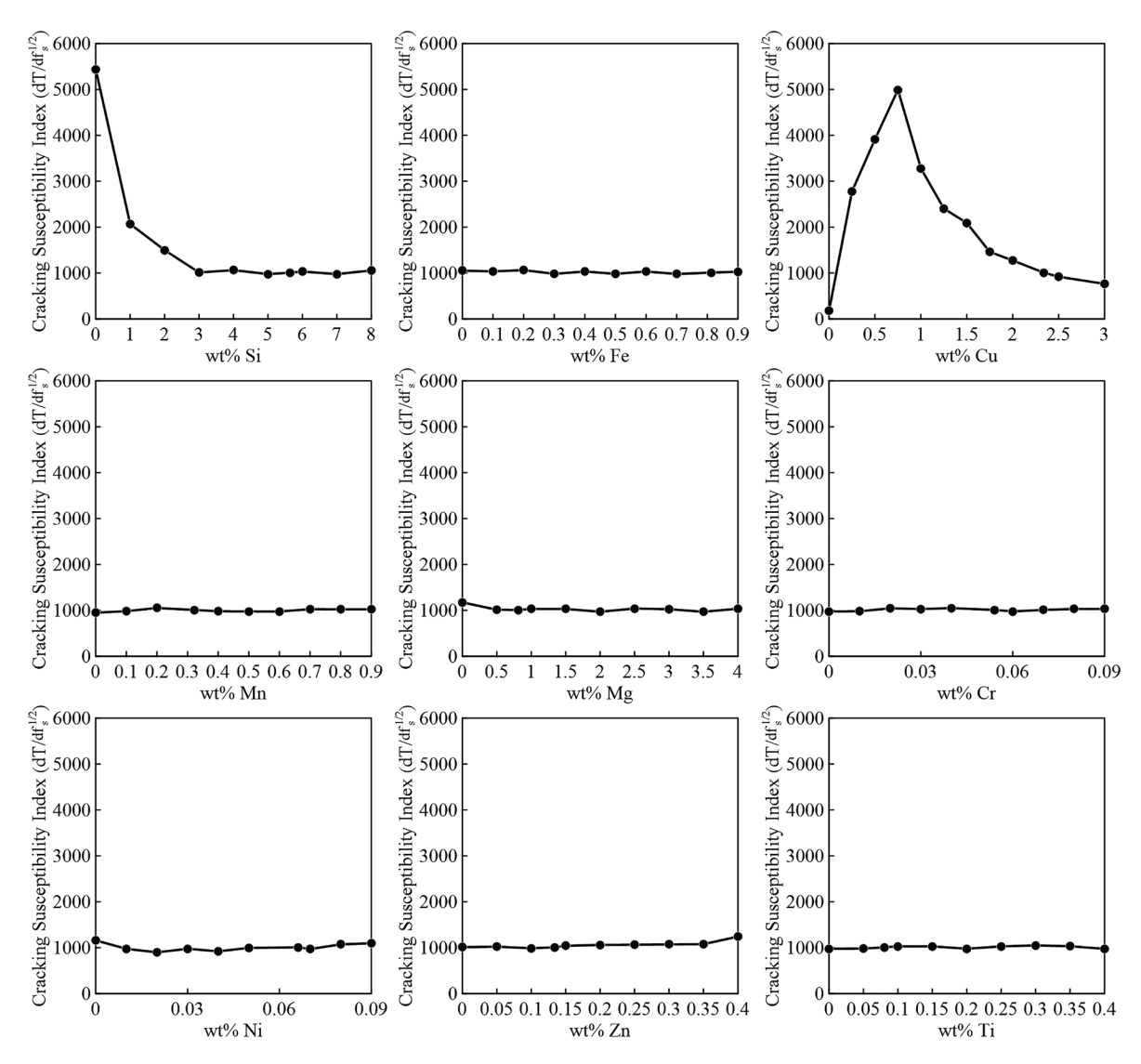


Fig. 2 — Crack susceptibility index of the average twitch composition with varying individual elemental contents.

Table 3 — The Composition of the Twitch Alloy Determined Through OES Analysis											
Al	Si	Fe	Cu	Mn	Mg	Cr	Ni	Zn	Ti	Residuals (Be, Sn, Ca)	
90.55	3.66	0.62	3.53	0.38	1.04	0.01	0.08	0.09	0.04	< 0.01	

feedstock for a fusion-based AM process, the solidification cracking susceptibility of the alloy must be evaluated (Ref. 23). Several high-strength aluminum alloys, particularly wrought aluminum compositions (Refs. 10, 23, 24), are prone to solidification cracking because of solidification shrinkage (the solid density is greater than the liquid density), thermal contraction, and physical constraints imposed by the rigid workpiece (Ref. 25). Therefore, avoiding this defect is crucial to developing a successful feedstock for AW-DED.

The goal of this work was to explore the composition space of the twitch scrap stream to identify a composition that

can be processed with AW-DED for structural applications. Thermodynamic simulations were used to determine a composition expected to exhibit low cracking susceptibility, and experimental wires were produced. Manual gas tungsten arc directed energy deposition (GTA-DED), a subset of AW-DED, was used to produce builds, and the builds underwent a series of heat treatments to evaluate microstructure evolution and age-hardening response. It is expected that this work will demonstrate that sustainability can be incorporated into the design process for welding and additive manufacturing fillers.

### **Methods**

## Composition of the Twitch Aluminum Scrap Stream

To evaluate the composition space of the scrap stream, 12 batches of twitch were analyzed with x-ray fluorescence. The compositions are shown in Table 1.

### **Thermodynamic Simulations**

All thermodynamic simulations were performed in Thermo-Calc using the TCAL9 database. Gulliver-Scheil simulations were conducted to predict the phases present during the solidification of the average twitch composition. Then, a series of Scheil simulations were performed to determine the influence of each element in twitch on solidification cracking susceptibility to select a crack-resistant composition. Single-axis-equilibrium phase fraction vs. temperature and Scheil simulations were performed for the chosen composition to confirm which phases are expected to be present. The single-axis equilibrium simulation was also used to identify appropriate temperatures for solutionizing and aging heat treatments.

## **Solidification Cracking Susceptibility Predictions**

Prior to beginning experimentation, a target composition was selected from the ranges in Table 1 based on its solidification cracking susceptibility. According to Kou, the solidification cracking susceptibility index (CSI) is related to the slope of a Gulliver-Scheil simulation at terminal solidification, according to Equation 1 (Ref. 26):

$$\left| \frac{\mathrm{dT}}{(\mathrm{df}_\mathrm{s})^{1/2}} \right| \mathrm{as} \ (\mathrm{f}_\mathrm{s})^{1/2} \to 1 \tag{1}$$

where T is the temperature and  $f_s$  is the volume fraction of the solid phase. The analysis is done toward the end of solidification, when  $f_s^{\frac{1}{2}}$  is between 0.85 and 0.99 (Ref. 23). The higher the value of  $\frac{dT}{|df_s|^{1/2}}|$ , the more likely the material will crack. The average composition of twitch was used as the baseline. Then, each element was varied individually according to the ranges in Table 1, while the other elements remained constant at the average composition. The selected composition was predicted to be least prone to solidification cracking.

### **Custom Wire Manufacturing**

The selected composition of the twitch alloy was replicated with a powder-core tubular wire produced from non-recycled material (Ref. 27). The wire was made using a 2024 Al-alloy strip sheath and a series of pre-alloyed powders detailed in Table 2. The wire was drawn down to 1.5–2 mm diameter for GTA-DED processing.

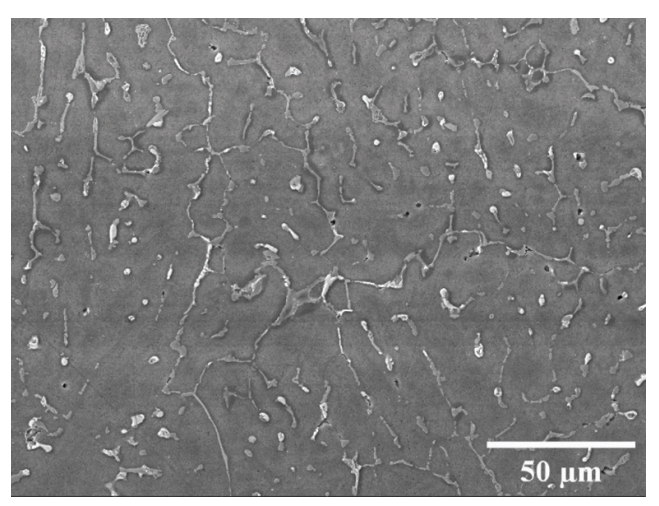


Fig. 3 — SEM SE micrograph of the GTA-DED build in the as-deposited condition showing Al dendrites with various constituents in the interdendritic regions. The microstructure was etched with a dilute HF solution prior to imaging.

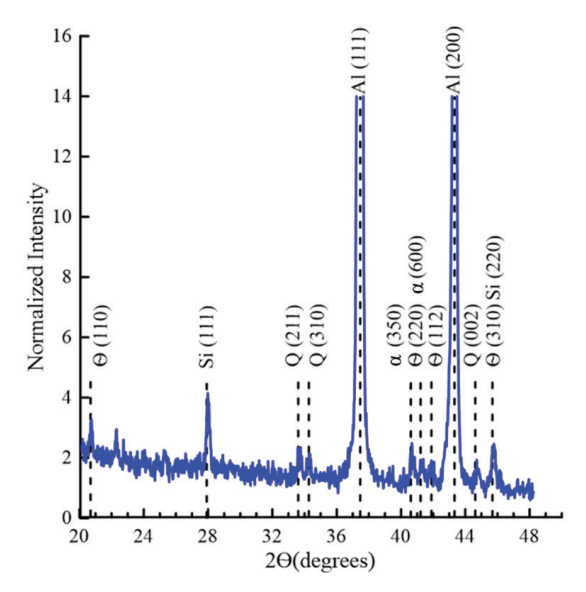


Fig. 4 — X-ray diffractogram of the AW-DED build in the as-deposited condition, indicating that  $\theta$ , Si, Q, Al, and  $\alpha$  were present.

### **GTA-DED Processing Parameters**

The powder core tubular wire feedstock was deposited on a 1100 Al plate using a manual Miller Dynasty gas tungsten arc welding heat source. During manual deposition, the current fluctuated between 50 and 150 A with an average heat source velocity of 2 mm/s. The builds were one-pass wide and measured approximately 25 mm tall, 50 mm long, and 13 mm wide.

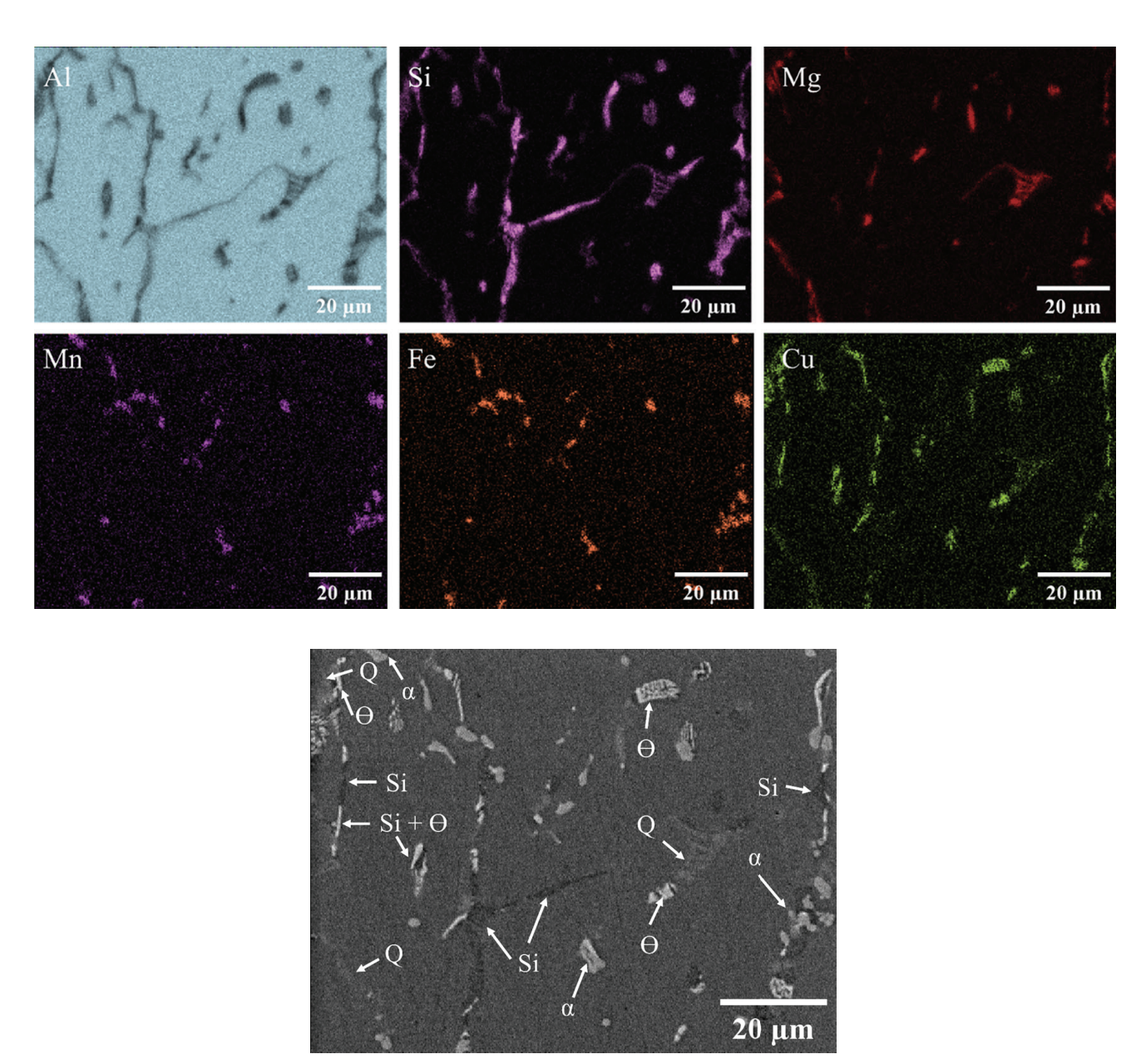


Fig. 5 — EDS map showing the concentrations of Al, Si, Mg, Mn, Fe, and Cu with respect to the SEM SE image indicating the expected phase based on composition.

### **Heat Treatments**

Heat treatments were conducted in a Carbolite open-air furnace preheated to the desired temperature. A K-type thermocouple was attached to each sample to record temperature. Solutionized samples were quenched in water prior to aging heat treatment.

### **Microstructure Characterization**

The builds were sectioned, mounted, and polished for characterization and hardness measurements. X-ray diffraction (XRD) using a Panalytical Empyrean with a Cu source operated at 20 kV and 40 mA was performed on polished

samples to determine the phases present after deposition and following heat treatment. A Tescan S8252G scanning electron microscope (SEM) with a beam energy of 15 keV was used for imaging and energy dispersive spectroscopy (EDS). SEM secondary electron (SE) imaging was performed on samples etched with a dilute (1:100) aqueous HF solution.

### **Hardness Testing**

The age-hardening response was evaluated via Vickers hardness testing before and after heat treatment. Samples were tested under 100 gmf with a 10-s dwell time and spacing of at least two indent widths apart in the as-built condition, the solutionized condition, and several aged conditions. Eighty hardness measurements were taken per condition.

Table 4 — (	Compositio	ons (wt-%)	of the Diffe	rent Phase	s Predicted	at the End	l of Solidific	ation in the	e GTA-DED	Build
Phase	Al	Si	Fe	Cu	Mn	Mg	Cr	Ni	Zn	Ti
α	59.2	10.9	0.3	_	29.6	_	< 0.1	_	_	_
θ	47.4	0.2	< 0.1	52.4	< 0.1	_	_	< 0.1	_	_
Si	< 0.1	100	_	_	_	_	_	_	< 0.1	< 0.1
Q	21.6	27.0	_	20.3	_	31.1	_	_	_	_
Al	93.6	0.85	< 0.1	4.2	< 0.1	0.4	< 0.1	< 0.1	0.9	< 0.1

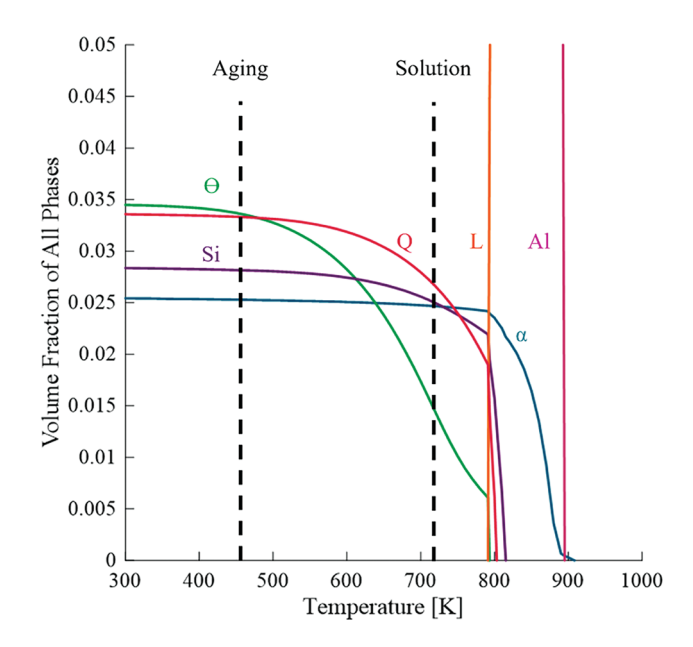


Fig. 6 — Predicted phase fraction as a function of temperature, including only phases that were experimentally observed in the as-deposited condition. The selected temperatures for solutionizing and aging experiments of 450°C (723 K) and 190°C (463 K), respectively, are shown.

### **Results**

# **Solidification Cracking Susceptibility Predictions for Composition Selection**

Gulliver-Scheil simulations of compositions within the twitch scrap stream were conducted, and the Kou CSI was used to determine which elements influenced cracking (Ref. 26). Figure 1 shows a Gulliver-Scheil simulation of the average twitch composition; a small amount of the  $\alpha$ -phase formed first, followed by Al. At terminal solidification, the phases expected were  $\alpha$ -Al(Fe, Mn)Si, Al, Q,  $\theta$ , and Si. Applying the Kou CSI to the various Gulliver-Scheil simulation results demonstrated that most of the elements listed in Table 1

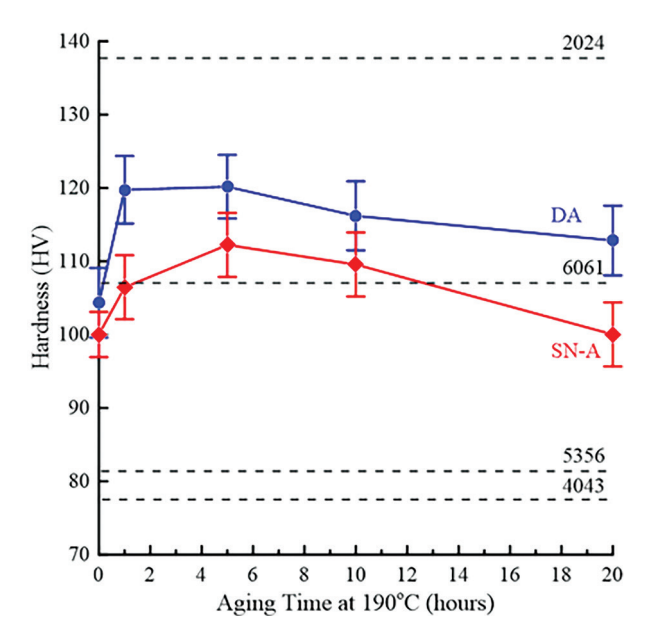


Fig. 7 — Evolution of hardness during solution-aging and direct aging heat treatments at 190°C. Error bars represent 95% confidence intervals.

did not significantly impact the CSI except for Si and Cu, as seen in Fig. 2. The CSI was highest around 0.75 wt-% Cu and 0 wt-% Si before decreasing with further increases in Cu and Si content. This behavior matched other Al alloys (Refs. 19, 26). Alloys like 2219 and 2319 contain elevated Cu content to reduce cracking susceptibility (Ref. 24). It has also been documented that solidification cracking in Al-Cu systems is highest between 0.7 and 1.2 wt-% Cu (Ref. 26). Increasing the Cu content beyond this range allows for backfilling of incipient cracks during solidification (Ref. 26). Figure 1 demonstrates that the final phases to form contained Cu, indicating that the liquid became enriched with Cu by the end of solidification, which promoted liquid backfilling between dendrites.

To avoid solidification cracking, the Cu content was targeted to be 2.5 wt-% Cu. The rest of the elements in the alloy were targeted to approximately the average compositions listed in Table 1. Wire was produced from this composition,

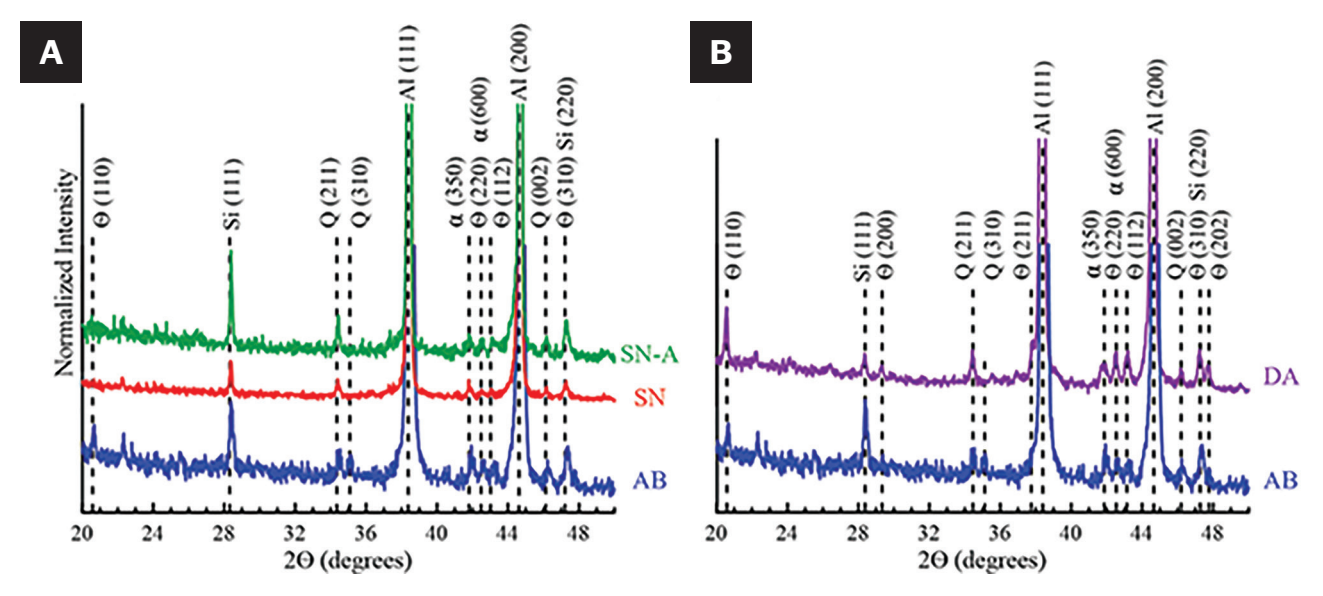


Fig. 8 — X-ray diffractograms of GTA-DED builds in the: A — As-built (AB), solutionized (SN), and solutionized peak-aged (SN-A 5 h) conditions; B - AB and direct aged (DA) 5-h conditions.

and GTA-DED builds were made. Optical emission spectroscopy analysis was performed on the builds. The results are in Table 3. Although the compositions of the elements in the build deviated from the targeted values due to challenges in the powder-core wire-making process, they did fall within the range of the twitch scrap stream, so the actual composition was expected to be representative.

One additional Scheil simulation was performed for the actual measured composition of the GTA-DED build shown in Table 3. Table 4 shows the phases and respective compositions expected at the end of solidification. By comparison to Fig. 1, the same phases expected at the end of the solidification in the average twitch scrap stream composition were expected in the actual twitch alloy. Predicted phase compositions will be used to facilitate phase identification in the microstructure using energy dispersive spectroscopy (EDS).

### Microstructure in the As-Deposited Condition

An SEM SE micrograph taken from the mid-height of the build in the as-deposited condition is shown in Fig. 3. The microstructure consisted of aluminum dendrites with various constituents in the interdendritic regions. According to the Gulliver-Scheil simulation shown in Fig. 1 and Table 4, the phases that were expected to be in the interdendritic regions were Si,  $\theta$ , and Q. The  $\alpha$ -phase was expected to be randomly distributed throughout the microstructure because a small amount forms first from the liquid. As predicted from the crack susceptibility calculations, no evidence of solidification cracking was observed in the builds.

A sample in the as-deposited condition was evaluated with XRD to determine what phases were present after deposition. The x-ray diffractogram in Fig. 4 shows peaks attributable to Al (majority phase) with lower intensity peaks associated with  $\alpha$ ,  $\theta$ , Q, and Si. The results generally

indicated that the phases predicted from thermodynamic simulations were present after deposition.

To help identify microstructural constituents in the interdendritic regions, EDS mapping results are shown in Fig. 5. Based on the predicted compositions in Table 4, constituents with elevated amounts of Al, Fe, Mn, and Si were indicative of  $\alpha$ -phase, while those high in Mg, Cu, and Si were indicative of Q-phase. Constituents with elevated Al, Si, and Cu, but low Mg, likely contain Si with  $\theta$  dispersed between lamellae (Ref. 17). There are some regions that showed primarily elevated Si and Mg, so it is possible that Mg2Si was present, although not predicted in the thermodynamic simulations, and also not identified in XRD. Based on these interpretations, the constituents in the SE SEM micrograph in Fig. 5 are labeled with the most likely phase based on composition.

As shown in Fig. 5, the dominant phase in the interdendritic regions appeared to be Si, while Q and  $\theta$  were less prominent. The  $\alpha$ -phase particles were randomly distributed throughout the microstructure, as expected. Some were round and clustered, while others were script-like or skeletal morphologies. The Q particles were large, and one toward the right side of the map was globular. The  $\theta$  precipitates primarily existed within the Si-rich constituents in the interdendritic regions and appeared to be present as both isolated round particles as well as fine lamellae.

### **Thermodynamic Predictions for Heat Treatment Selection**

A single-axis equilibrium simulation of phase content as a function of temperature (Fig. 6) was performed to determine heat-treating temperatures. Only phases that were experimentally observed in the as-deposited condition were included in the simulation. There is no temperature below which liquid forms where Al is the only solid phase, which

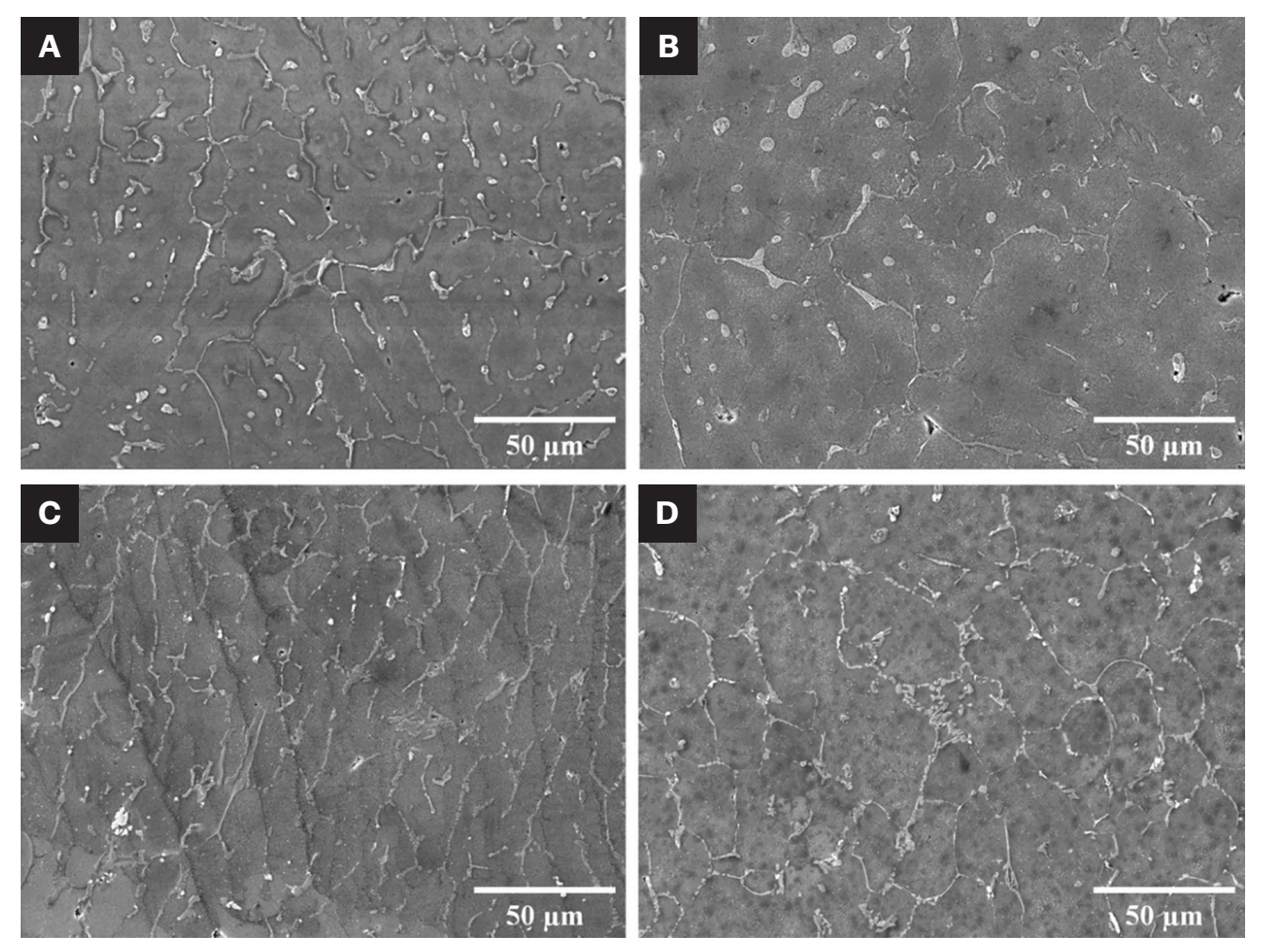


Fig. 9 — SEM SE micrographs of the: A — As-built; B — direct-aged peak aged (5 h); C — solutionized; and D — solution-aged peak aged (5 h).

would be ideal for selecting a solution heat-treating temperature. Instead,  $450^{\circ}\text{C}$  ( $723\,\text{K}$ ) was chosen for the solutionizing temperature because a considerable amount of  $\theta$ , and to a lesser degree Q, could be dissolved. Figure 6 also shows that below  $200^{\circ}\text{C}$  ( $473\,\text{K}$ ), the amount of many of the secondary phases plateaus with decreasing temperature. Therefore, an aging temperature of  $190^{\circ}\text{C}$  ( $463\,\text{K}$ ) was chosen for aging experiments in alignment with aging studies on similar alloys in the literature (Ref. 28). Based on Fig. 6, the phases that increased in amount the most from the solution heat treating temperature to the aging temperature were  $\theta$  and, to a lesser degree, Q. It is expected that the non-equilibrium precursor phases to  $\theta$  will be largely responsible for the potential aging response with the non-equilibrium precursor phases to Q making a minor contribution as well.

### **Age-Hardening Response**

Hardness as a function of aging time for samples that were not solution heat-treated (direct-aged) and samples that were solution heated prior to aging (solution-aged) is shown in Fig. 7. For the solution-aged samples, the hardness at 0 aging time was the solution heat-treated condition (450°C for 1h).

For the direct-aged samples, the hardness at O aging time represented the hardness in the as-built condition. Both the solution-aged and direct-aged samples showed a maximum in hardness as a function of aging time, indicating that the data shown in Fig. 7 encompassed underaged, peak aged, and overaged conditions. However, the decrease in hardness with increasing time was more subtle with the directed-aged condition compared to the solution-aged condition. In both aging conditions, the 5-h aging treatment had the highest increase in hardness, and the difference in peak hardness values between the two aging conditions was not statistically significant. However, for the shortest aging time of 1 h, the direct-aged sample did show a higher hardness than the solution-aged sample, which is statistically significant. For comparison, hardness values of commercial precipitation hardened aluminum alloys 2024 and 6061 are indicated in Fig. 7. Similarly, the hardness of commonly used aluminum alloy filler materials, 5356 and 4043, which are used for welding 6061 because they are not prone to solidification cracking (Ref. 29), are shown as well. The peak hardness values of the GTA-DED twitch-derived composition in both aging conditions was between 6061 and 2024 and well above those of 5356 and 4043. The twitch alloy displayed hardness values

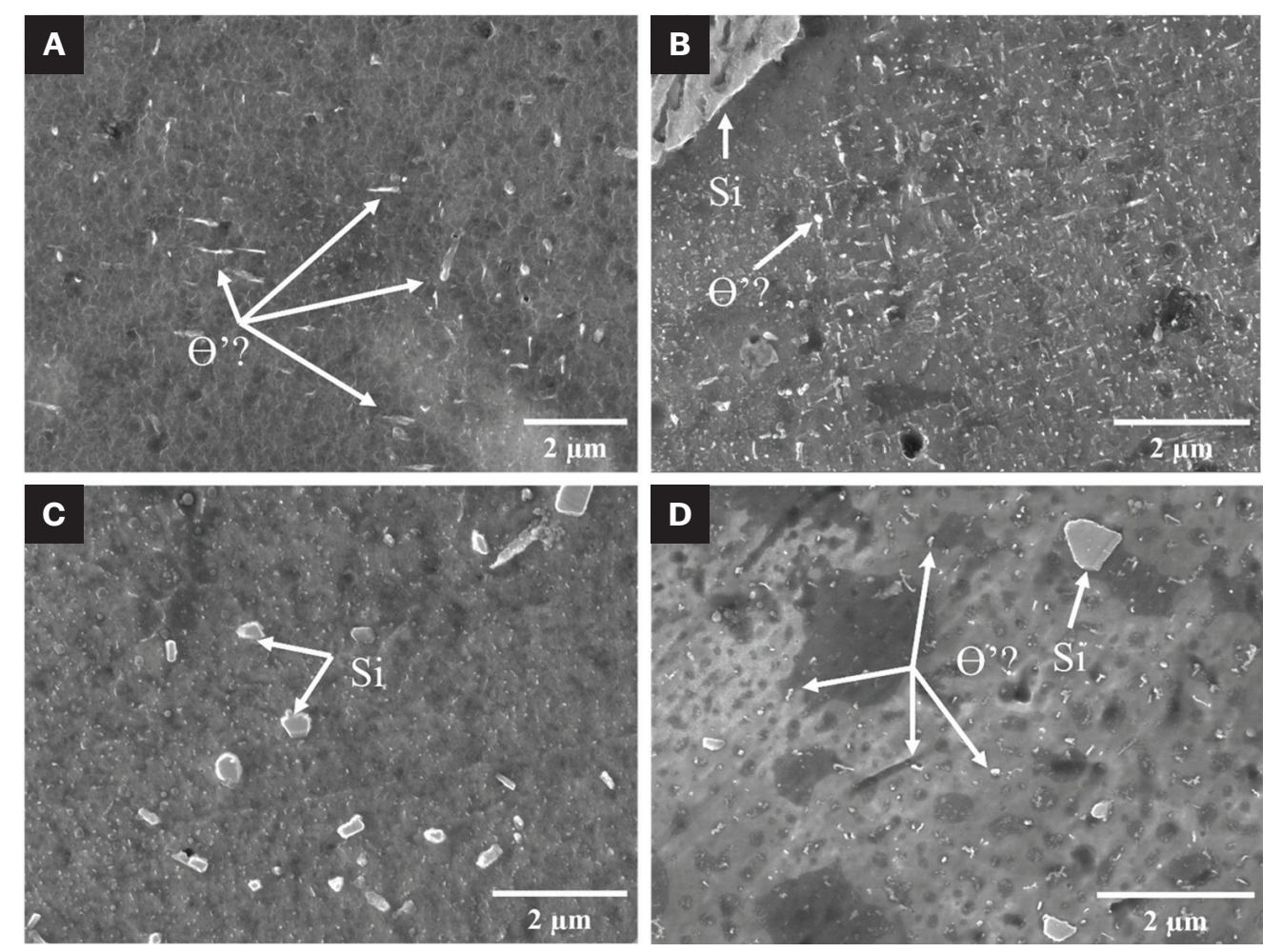


Fig. 10 - Higher magnification SEM SE micrographs focusing on fine precipitates in the GTA-DED builds: A -As-built; B - direct-aged peak aged (5 h); C - solutionized; D - solution-aged peak aged (5 h) conditions.

that would be attractive for welding and additive manufacturing applications relative to existing weldable aluminum-based filler materials.

### **Microstructure Evolution During Aging**

Additional characterization was performed on samples during aging to understand the microstructural changes concomitant with the observed hardening response in the solution-aged and direct-aged conditions. X-ray diffractograms of samples in the as-built, solution heat-treated, and peak solution-aged (5 h at 190°C) are shown in Fig. 8A. Relative to the as-built condition, the solution heat-treated sample showed a decrease in the Si (111) peak intensity. In the peak solution-aged condition, the peak intensity increased again. According to thermodynamic simulations in Fig. 6, the amount of the Si phase should have increased by a small amount between solution heat treating and aging. Still, this change is challenging to quantify because only one unique peak from Si was observable. The intensities of many of the  $\theta$  peaks decreased in the solution heat-treated condition and then increased again during peak aging, which was predicted from thermodynamic simulations.  $\theta$ 

was the only phase that changed appreciably in amount in the temperature range between solution heat treating and aging considered here. The peak intensities of  $\alpha$  and Q also changed to a small degree between solution heat treating and aging; however, these phase amounts were not expected to vary much according to thermodynamic simulations. Figure 8B shows diffractograms of the as-built and peak direct-aged conditions. The primary change that was observable in the peak aged condition was that many of the  $\theta$  peaks increased in relative intensity. A shoulder on the left side of the Al (111) peak also appeared in the peak aged condition, which could have been the  $\theta$  (211) peak. Overall, the phase that showed the most distinct change during aging heat treatment was the  $\theta$  phase for the solution-aged and direct-aged conditions, although the changes were somewhat subtle.

SEM SE micrographs of as-built, solution heat-treated, and peak aged for the solution-aged samples are shown in Figs. 9A, C, and D, respectively. In general, the coarser constituents in the interdendritic regions did not appear to be affected by the sequence of heat treatments. However, there was an increase in the number of finer precipitates in the dendrite core regions in the peak aged condition compared to the solution heat-treated condition. Figure 9B shows the microstructure of the peak direct-aged condition. Like the solution-aged condition, the direct-aged condition showed fine precipitation within the dendrite cores, with the coarser constituents in the interdendritic region essentially unaffected.

Higher magnification micrographs focusing on the evolution of the finer precipitates are shown in Fig. 10. In the as-built condition (Fig. 10A), there were a few finer precipitates of spherical and plate-like morphologies. After solution heat treating, the Si particles near the interdendritic regions were still present, but the finer precipitates seen in the as-built condition were not present, as shown in Fig. 10C. In the peak hardness solution-aged condition, fine precipitates were again observed, except they were finer and more uniformly distributed compared to the as-built condition, as shown in Fig. 10D. As for the peak hardness direct-aged condition, the fine precipitates were coarser with a higher number density compared to the solution aged condition, and they appeared to be arranged in orthogonal arrays (Fig. 10B). In all the images in Fig. 10 where fine precipitates were observed, a greater amount was present surrounding Si precipitates near the interdendritic regions compared to the dendrite core areas. It is likely that the elements that formed the fine precipitates segregated to the interdendritic regions during solidification, so higher amounts of the precipitates formed in these regions during aging.

The fine precipitates shown in Fig. 10 were too small for effective EDS measurements, so it could not be conclusively confirmed that they were rich in Cu and were likely  $\theta,\theta',$  or  $\theta''.$  Transmission electron microscopy (TEM) would be needed to fully characterize these precipitates. XRD did show that the intensity of  $\theta$  peaks increased at peak hardness for the solution-aged and direct-aged conditions, and the fine precipitates showed higher number density at peak hardness, so the precipitates were likely  $\theta$  or some intermediate phase leading to  $\theta$ , such as  $\theta'$  or  $\theta''$ , which could not be conclusively distinguished in XRD.

### **Discussion**

## **Comparison of Thermodynamic Predictions** and **Experimental Results**

Strong agreement between thermodynamic simulations and experimental results was observed in the phases displayed by the twitch-derived alloy during solidification. The solidification cracking susceptibility modeling accurately predicted low solidification cracking susceptibility as there were no solidification cracks seen through the height of the build. However, weldability testing focusing on solidification cracking will be evaluated in the next stage of this work. Gulliver-Scheil simulations accurately predicted the phases that existed in the interdendritic regions: Si, Q, and  $\theta$ . The Mg/Si content was less than 1; therefore, the formation of  $\theta$  and Q was more thermodynamically favorable than the formation of other possible Mg-containing phases (Ref. 30). Si and Q precipitates acted as nucleation sites for  $\theta$  because interdendritic liquid highly concentrated with Cu surrounds these precipitates (Refs. 5,

28, 31). The presence of these phases was confirmed by XRD results, and EDS measurements facilitated identifying their location in the interdendritic regions. The first phase to solidify,  $\alpha$ -Al(Fe,Mn)Si, was observed throughout the microstructure, as would be expected from a primary phase that forms before a majority phase during solidification.

The results from heat treatments also had strong agreement with thermodynamic predictions. The solutionizing temperature was predicted to significantly decrease the amount of  $\theta$ , which aligned with XRD data. Additionally, a slight decrease was predicted in the amount of Si and Q from solution heat treating, which was also corroborated by XRD results. Aging heat treatments were predicted to primarily result in increases in  $\theta$  and, subsequently, harden the alloy. The intensity of peaks attributed to  $\theta$  in XRD were found to increase after aging, again supporting thermodynamic predictions. Fine elongated precipitates that formed in orthogonal arrays were observed in the peak direct-aged condition but not observed in the solution heat-treated condition, further supporting the possibility that  $\theta$  or  $\theta$ ' formed during aging and contributed to the hardening response. There may have been an additional contribution to strengthening from other non-equilibrium precursor phases like GPZs or  $\theta$ " which could not be observed in the XRD results. If such phases were present and contributing to the strengthening, TEM would be required to detect them.

## **Strengthening Contributions in Peak Aged Conditions**

Solutionizing the AW-DED processed twitch alloy at 450°C for 1 h decreased the amount of  $\theta$ , Si, and Q, according to the XRD data. The microstructures in Figs. 9 and 10 show that while there were still precipitates present in the solutionized sample, some precipitates did dissolve. The hardness of the solutionized sample decreased relative to the as-built condition, which may be attributed to fewer precipitates in the microstructure as well as some reduction in dislocation density. Solutionizing for more time may have higher efficiency in completely dissolving  $\theta$  precipitates and induce a greater strengthening effect. The hardness data for the solution-aged samples showed that 5 h at 190°C was most effective for hardening the solutionized samples. The XRD data for solution peak aged conditions showed an increase in peak intensity for  $\theta$ , Si, and the Q phases relative to the solution heat-treated condition, indicating that these phases may have contributed to the hardening response. Phase fractions were not quantified from the XRD data; however, thermodynamic predictions suggest that the largest increase in phase amount from aging should be from the  $\theta$  phase and should, therefore, be the biggest contributor to strengthening. Furthermore, fine precipitates were observed in the as-deposited condition, absent in the solution heat-treated condition, and present in a finer distribution after peak aging. These precipitates were likely  $\theta$ ,  $\theta$ ', or  $\theta$ " and likely had the greatest impact on strengthening. Strengthening contributions from precipitates that were too fine to resolve with the technique employed here (e.g. GP zones) cannot be completely discounted.

The highest hardness condition was observed after direct aging at 190°C for 5 h. The greatest changes in XRD peak

intensities occurred in every peak associated with  $\theta$  in the direct peak aged condition. In fact, additional  $\theta$  peaks in the direct-aged condition were identified in comparison to the as-built condition. In the direct peak aged condition, fine precipitates, similar to the ones observed in the solution peak aged condition, were observed. However, the fine precipitates in the peak direct-aged condition appeared to have a higher number density, which could explain the higher hardness in this condition. Similar to the solution peak aged condition, the phase most likely responsible for hardening was  $\theta$  or, more likely,  $\theta$ ' based on aging experiments on other Cu-bearing Al alloys (Refs. 18-20, 32).

Direct-aging had a more substantial impact on hardness than the solution-aging experiments. During the GTA-DED building process, cyclic heating and cooling likely introduced thermal strains that resulted in plastic deformation and, therefore, a higher dislocation density. The dislocation density present in the as-deposited condition was likely reduced during solution heat treating, resulting in fewer nucleation sites for  $\theta$  or  $\theta$ ' to form during aging. The fewer nucleation sites in the solution peak aged condition could explain the lower number density and lower hardness compared to the direct peak aged condition.

The morphology of the fine precipitates observed in the peak aged conditions aligned with the morphology of  $\theta$ ' documented in literature (Ref. 33), and the highest strengthening in Al-Cu alloys comes from  $\theta^{\prime}$  precipitates (Ref. 34). However, these fine precipitates were too small to make SEM EDS measurements to confirm their composition. The only way to measure their composition would be EDS in a TEM, which was not performed here. Additionally, diffraction could be performed in the TEM to determine the crystal structure of the fine precipitates. In every aged condition depicted in Fig. 10, the small precipitates surrounded Si-rich precipitates near the interdendritic regions. The interdendritic regions were also known to be concentrated with Cu in the as-built condition, according to the EDS in Fig. 5. There may have been Cu-rich precursor phases (GPI zone, GPII zone) surrounding the Si that were undetectable which may have promoted  $\theta$ ' formation in these regions during aging. Once again, the only way to evaluate the presence of additional Cu-rich precipitates that could be contributing to the strengthening is to use TEM.

### **Conclusions**

A combination of thermodynamic simulations and experiments were performed to select an alloy from the twitch aluminum scrap stream to be used as a wire feedstock for GTA-DED. Predictions of solidification cracking susceptibility were performed to select a composition that should minimize cracking during deposition, and additional simulations were performed to select heat treatments for age-hardening. Wire feedstocks of the selected alloy were produced, and GTA-DED builds were made and characterized. Based on the results, the following conclusions are made:

■ Cu content was predicted to have the greatest effect on crack susceptibility within the twitch composition space, with the greatest susceptibility at approximately 1 wt-% Cu, which is consistent with other Al-Cu alloys. A higher Cu content

of 2.5 wt-% was chosen for experimentation to minimize solidification cracking susceptibility.

- There was good agreement between the phases observed after GTA-DED deposition and those predicted with Gulliver-Scheil simulations. The microstructure consisted of aluminum dendrites with Si,  $\theta$ , and Q in interdendritic regions and  $\alpha$ phase dispersed throughout the microstructure.
- Based on thermodynamic simulations, a solution heat treating temperature of 450°C should cause a significant portion of  $\theta$  to dissolve and reform during aging at 190°C, which matched experimental results.
- Samples that were peak aged after solution heat treatment and direct peak aged showed increases in the  $\theta$  phase according to XRD and the development of fine precipitates in the microstructure. The peak hardness values of the twitch alloy were comparable to the commercial alloy 6061, indicating there is promise for the use of a twitch-derived alloy in structural
- The  $\theta$  phase and the precursor  $\theta$ ' phase could not be distinguished with the techniques employed here, but it is likely that the fine precipitates responsible for the agehardening response were  $\theta$ ', similar to other Al-Cu alloys.
- The results of this work show that alloys with desirable combinations of processability and mechanical performance can be designed from scrap streams, which opens new opportunities to improve the sustainability of many alloy classes.

### Data Availability

The raw/processed data required to reproduce these findings cannot be shared at this time as the data also forms part of an ongoing study. However, reasonable requests for data will be accommodated by contacting the corresponding author.

### Acknowledgments

The authors acknowledge support from the Center for Advanced Non Ferrous Structural Alloys, (CANFSA), a National Science Foundation Industry University Cooperative Research Center (IUCRC).

The authors acknowledge Valimet for providing Al-Si and 2024 alloyed powders for this project.

### **Funding**

Jamie Hamilton was supported by the U.S. Department of Education under a Graduate Assistance in Areas of National Need (GAANN) Fellowship (Grant # P200A210134).

This material is based upon work supported by the National Science Foundation under Grant Number (2137243). Data analysis was supported by instrumentation that was acquired through the support of the National Science Foundation (DMR-1828454). Any opinions, findings, and conclusions or recommendations expressed in this material are those of the author(s) and do not necessarily reflect the views of the National Science Foundation.

#### References

- 1. Williams, K. 2023. Classification of shredded aluminum scrap metal using magnetic induction spectroscopy. *Sensors* 23(18): 7837.
- 2. Milligan, B. et al. 2024. Upcycling of mixed aluminum alloy shredder scrap using shear processing. *Advanced Materials & Processes* 182(5): 15–20.
- 3. Raabe, D. et al. 2022. Making sustainable aluminum by recycling scrap: The science of "dirty" alloys. *Progress in Materials Science* 128(7).
- 4. Taylor, J. 2012. Iron-containing intermetallic phases in Al-Si based casting alloys. 11th International Congress on Metallurgy & Materials SAM/CONAMET 2011.
- 5. Mondolfo, L. 1976. *Aluminum Alloys: Structure & Properties*. Butterworth-Heinemann.
- 6. Rajakumar, J. 2022. ISRI specs: Twitch-floated fragmentizer aluminum scrap. Retrieved from *recycleinme.com/scrap-news/newsdetails-782*.
- 7. Ebhota, W. 2018. "Intermetallics formation and their effect on mechanical properties of Al-Si-X alloys." In *Intermetallic Compounds Formations and Applications*. IntechOpen.
- 8. Gao, T. 2017. Morphological evolution and strengthening behavior of  $\alpha$ -Al(Fe,Mn)Si in Al–6Si–2Fe–xMn alloys. *Results in Physics* 7: 1051–1054.
- 9. Pan, Q. 2023. Phase transformation and microstructural evolution in Al-Mn-Fe-Si 3104 aluminum alloy made by laser directed energy deposition. *Additive Manufacturing* 77.
- 10. Pan, Q. 2024. High-throughput compositional study of 3xxx Al alloy using laser synthesis and small-scale rolling: A case study. *Light Metals* 2024.
- 11. Cooper, M. 1967. The crystal structure of the ternary alloy  $\alpha(Al-FeSi)$ . *Acta Crystallographica* 23: 1106–1107.
- 12. Grasserbauer, J. 2021. Influence of Fe and Mn on the microstructure formation in 5xxx alloys—Part I: Evolution of primary and secondary phases. *Materials* 14(12).
- 13. Que, Z. 2018. Formation of the Fe-containing intermetallic compounds during solidification of Al-5Mg-2Si-0.7Mn-1.1Fe Alloy. *Metallurgical and Materials Transactions A* 49(6): 2173–2181.
- 14. Salmi, S. 2024. Understanding off-stoichiometry of Q-phase in Al-Cu-Mg-Si alloys. *Scripta Materialia* 248.
- 15. Kim, K. 2018. Energetics of native defects, solute partitioning, and interfacial energy of Q precipitate in Al-Cu-Mg-Si alloys. *Acta Materialia* 154: 207–219.
- 16. Gazizov, M. 2019. Precipitation behavior in an Al–Cu–Mg–Si alloy during ageing. *Materials Science and Engineering: A* 767(8): 138369.
- 17. Zobac, O. 2020. Experimental isothermal sections of the ternary phase diagram Al–Cu–Si at  $600^{\circ}$ C and  $800^{\circ}$ C. *Journal of Materials Science* 55(31).
- 18. Hu, X. 2022. Repurposing the  $\theta$  (Al2Cu) phase to simultaneously increase the strength and ductility of an additively manufactured Al–Cu alloy. *Materials Science and Engineering:* A 850: 143511.
- 19. Bourgeois, L. 2011. Structure and energetics of the coherent interface between the  $\theta$ ' precipitate phase and aluminium in Al–Cu. *Acta Materialia* 59(18): 7043–7050.
- 20. Gao, L. 2021. The growth mechanisms of  $\theta$ ' precipitate phase in an Al-Cu alloy during aging treatment. *Journal of Materials Science & Technology* 61: 25–32.
- 21. Liu, L. 2014. The effect of Si on precipitation in Al–Cu–Mg alloy with a high Cu/Mg ratio. *Materials Science and Engineering:* A 606: 187–195.
- 22. Li, Y. 2022. Comprehensive review of wire arc additive manufacturing: Hardware system, physical process, monitoring, property

- characterization, application and future prospects. Results in Engineering 13.
- 23. Kou, S. 2015. A criterion for cracking during solidification. *Acta Materialia* 88: 366–374.
- 24. Huang, C. 2004. Liquation cracking in full-penetration Al-Cu welds. Welding Journal 83(2): 50-s to 58-s.
- 25. Soysal, T. 2019. Effect of filler metals on solidification cracking susceptibility of Al alloys 2024 and 6061. Journal of Materials Processing Technology 266: 421–428.
  - 26. Kou, S. 2020. Welding metallurgy. Wiley
- 27. Hillier, C. 2010. Powder-cored tubular wire development for electron beam freeform fabrication. M.S. thesis, Colorado School of Mines.
- 28. Mohamed, A. 2022. Intermetallics formation during solidification of Al-Si-Cu-Mg cast alloys. *Materials* 15(4).
- 29. Coniglio, N. 2008. Defining a critical weld dilution to avoid solidification cracking in aluminum. *Welding Journal* 87(9): 237-s to 247-s.
- 30. Chakrabarti, D. 1998. Precipitation in Al-Mg-Si-Cu alloys and the role of the q phase and its precursors. *Automotive Alloys II*: 27–44.
- 31. Sediako, D. 2011. Solidification analysis of Al-Si alloys modified with addition of Cu using in-situ neutron diffraction. *NRC Publications Archive*.
- 32. Płonka, B. 2023. Influence of copper content on the structure and properties of aluminum alloys. *Archives of Civil and Mechanical Engineering* 24.
- 33. Chen, Z. 2021. Theoretical and experimental study of precipitation and coarsening kinetics of  $\theta'$  phase in Al–Cu alloy. *Vacuum* 189.
- 34. Wang, S. 2019. Crystal structures of  $Al_2Cu$  revisited: Understanding existing phases and exploring other potential phases. *Metals* 9(10).
- 35. Liu, J. 2016. Crack susceptibility of binary aluminum alloys during solidification. *Acta Materialia* 110: 84–94.

JAMIE HAMILTON and JONAH KLEMM-TOOLE (jklemmto@mines.edu) are with the Colorado School of Mines, Golden, Colo. JOHN E. CARSLEY is with Novelis, Kennesaw, Ga.